Nano Energy 77 (2020) 105299

Contents lists available at ScienceDirect

Nano Energy

journal homepage: http://www.elsevier.com/locate/nanoen

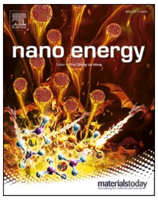

Unveiling the microscopic origin of asymmetric phase transformations in (de)sodiated Sb_2Se_3 with *in situ* transmission electron microscopy

Yi Wu[a,1], Wen Luo[b,1], Peng Gao[c], Chongyang Zhu[a], Xiaobing Hu[d], Ke Qu[c], Jing Chen[e], Yuqiao Wang[f], Litao Sun[a,*], Liqiang Mai[b,**], Feng Xu[a,***]

[a] *SEU-FEI Nano-Pico Center, Key Laboratory of MEMS of Ministry of Education, Southeast University, Nanjing, 210096, China*
[b] *State Key Laboratory of Advanced Technology for Materials Synthesis and Processing, Wuhan University of Technology, Wuhan, 430070, China*
[c] *Electron Microscopy Laboratory, International Centre for Quantum Materials, School of Physics, Peking University, Beijing, 100871, China*
[d] *Department of Materials Science & Engineering and NUANCE Center, Northwestern University, Evanston, IL, 60208, USA*
[e] *School of Electronic Science and Engineering, Southeast University, Nanjing, 210096, China*
[f] *School of Chemistry and Chemical Engineering, Southeast University, Nanjing, 211189, China*

ARTICLE INFO

Keywords:
Sb_2Se_3 nanowires
Contact interfaces
Ionic transport
In situ transmission electron microscopy
Sodium-ion battery

ABSTRACT

Sodium-ion batteries (SIBs) have huge application potential in large-scale energy storage systems due to high abundance and low cost of sodium resource. Metal chalcogenides, which store Na ions by multiple reactions of intercalation, conversion, and alloying, are considered promising anode materials with high theoretical capacity but often suffer from fast capacity fading and underlying reason remains elusive due to the lack of a precise understanding of microscopic behaviors. Here, combined with *in situ* high-resolution transmission electron microscopy and consecutive electron diffraction, we tracked phase transformations during (de)sodiation of Sb_2Se_3 nanowires in real time and revealed multi-step reaction mechanisms. During sodiation, Sb_2Se_3 NWs firstly underwent the intercalation of Na ions and forming $Na_xSb_2Se_3$ phase, following by the conversion reaction into Na_2Se and Sb phases; afterwards, metallic Sb could further alloy with Na to form Na_3Sb phase via sequential intermediate Na_xSb phases. While during desodiation, despite the reversible dealloying of Na_3Sb phase, the following deconversion of Na_2Se and Sb phases back to Sb_2Se_3 phase was incomplete, which is deemed to be the key factor causing rapid capacity decay. Furthermore, we reveal that contact interfaces between NWs greatly affected the degree of deconversion reaction due to possibly changed electrode reaction kinetics. This work not only reports the first experimental visualization proof showing the effect of contact interfaces on phase transformations of electrode materials, but also affords new insights into capacity decay mechanisms and rational design of high-capacity SIBs.

1. Introduction

Although lithium-ion batteries (LIBs) have been widely used as power sources for electronic devices and renewable power stations in decades [1,2], great concerns about the scarcity of lithium resources have accelerated the search for a viable and reliable alternative to LIBs. Recently, sodium-ion batteries (SIBs) have aroused extensive research interests from scientific and industrial communities due to high natural abundance and low cost of sodium resources. As a cognate element to lithium, sodium has similar physicochemical properties to lithium and thus SIBs practically share the same operating principle as LIBs [3–10]. At present, the severe capacity fading is one of the dilemmas suffered by SIBs, as the larger ionic radius of Na^+ results in slower diffusion kinetics and worse structural degradation of the electrodes [11,12]. Therefore, one of the main challenges to realize the practical application of SIBs is to deeply understand sodium storage mechanisms in such electrode materials, and thus to find and design suitable electrode materials with long-term cycling stability and high capacity.

---

[*] Corresponding author.
[**] Corresponding author.
[***] Corresponding author.
E-mail addresses: slt@seu.edu.cn (L. Sun), mlq518@whut.edu.cn (L. Mai), fxu@seu.edu.cn (F. Xu).
[1] These authors contributed equally to this work.

https://doi.org/10.1016/j.nanoen.2020.105299
Received 18 July 2020; Received in revised form 13 August 2020; Accepted 15 August 2020

By combining multiple mechanisms of intercalation, conversion, and alloying reactions to store energy, metal chalcogenides are considered the promising SIB anode materials with relatively high theoretical capacity [13,14]. For instance, antimony selenide (Sb_2Se_3), as one member of the chalcogenides, has demonstrated its superior electrochemical performance in SIBs. Owing to higher electrical conductivity of selenium (1×10^{-3} S m^{-1}) than that of sulfur (5×10^{-28} S m^{-1}) [15], Se-based compounds is expected to provide good electrode conductivity, resulting in a better rate capability [16]. Moreover, as-formed antimony can undergo further alloying reactions upon subsequent sodiation, which is very attractive due to its intrinsically higher energy capacity compared to traditional carbonaceous materials [17]. Theoretically, 1 mol of Sb_2Se_3 in a SIB system can generally react with 12 mol Na ions to form Na_2Se and Na_3Sb for a high capacity of 670 mA h g^{-1} [18]. Although the multistep reaction mechanisms can provide promising high energy density in SIBs [19,20], fast capacity decay in Sb_2Se_3 anodes limits further practical utilization. Depressingly, underlying reasons of capacity fading have not been fully understood due to the lack of a precise understanding of microscopic behaviors.

In situ transmission electron microscopy (TEM) technique has been recognized as a powerful tool to track electrochemical reactions of electrode materials on the nanometer scale in real time [21–27]. Herein, we construct an all-solid nano-battery based on individual Sb_2Se_3 nanowires (NWs) inside a TEM to enable direct visualization of the morphological and structural evolutions during (de)sodiation cycles. Upon initial sodiation, the reaction fronts (RFs) propagated along the longitudinal direction in the form of V-shape. Meanwhile, high-resolution imaging discerned two distinct reaction interfaces along the longitudinal and lateral directions, respectively. Consecutive electron diffraction (ED) sampling reveals that Sb_2Se_3 NWs underwent a three-step phase transformation during the first sodiation stage. Sodium ions were firstly intercalated into Sb_2Se_3 NWs, forming $Na_xSb_2Se_3$ phase; afterwards, further Na intercalation initiated the conversion reaction, resulting in the formation of Na_2Se and Sb phases; further, Sb could alloy with Na to form Na_3Sb phase via sequential intermediate Na_xSb phases. While during desodiation, although the dealloying of Na_3Sb was reversible, the incomplete conversion of Na_2Se and Sb phases back to Sb_2Se_3 was deemed to be key factor causing rapid capacity decay. The different degree of desodiaiton was found to originate from unstable contact interfaces of NWs that cause changed electrode reaction kinetics. This new finding underlies the significance of interface engineering in a real battery, particularly with multistep reaction mechanisms, in which electronic and ionic conduction depends greatly on steady contact interfaces of electrode nanostructures. Our work not only reports the first experimental visualization proof of the effect of contact interfaces on phase evolutions of electrode materials, but also affords valuable insights into capacity decay mechanisms and rational design of high-capacity SIBs with long cycling life.

2. Experimental section

2.1. Materials preparation

Sb_2Se_3 NWs were prepared through a facile hydrothermal process with slight modification [28,29]. In brief, 0.2 mM of $Sb(CH_3COO)_3$ and 0.3 mM of Na_2SeO_3 were dissolved in 75 mL of distilled water under stirring. Then 1.92 mM of hydrazine hydrate (80 wt%) was added drop-wise under constant stirring. Subsequently, the mixed solution was transferred into a 100 mL-capacity Teflon-lined autoclave that was sealed, heated, and maintained at 120 °C for 36 h. After the hydrothermal reaction, the as-obtained product was filtered and washed with distilled water and alcohol several times, and ultimately dried in vacuum at 70 °C for 12 h.

2.2. *In situ* electrochemical sodiation/desodiation experiments

The aberration-corrected transmission electron microscope (TEM, FEI Titan 80–300 kV) with a fast responding charge-coupled device (CCD) camera was used for *in situ* observation of the electrochemical reactions of Sb_2Se_3 NWs, including real-time imaging, consecutive electron diffraction (ED) sampling, and energy dispersive X-ray spectroscopy (EDS) mapping. The TEM is equipped with a Gatan high angle annular dark field (HAADF) detector for incoherent Z-contrast imaging. To construct the nanosized SIBs, Sb_2Se_3 NWs were attached to an Au rod by Ga–In liquid metal (with a liquidus temperature of 15 °C) as working electrode, and bulk metal Na scraped onto tungsten (W) probe was used as the counter electrode and Na source. The naturally oxidized Na_2O layer during transferring the sample holder into TEM acted as the solid electrolyte. The W probe was driven by a piezo-positioner in a Nanofactory TEM-scanning tunneling microscopy (STM) holder to make the Na_2O/Na and NWs contact. Once the contact was made, the electric biasing would be applied to intercalate/de-intercalate Na ions into/from the NWs and thus enable electrochemical sodiation/desodiation reactions that could be recorded for subsequent analysis.

2.3. Electrochemical measurements

The electrochemical performance was evaluated by the assembly of 2016-type coin cells in a glove box filled with pure argon gas. The comparison conventional electrodes were prepared by a mixed slurry with a weight ratio of 70% Sb_2Se_3 nanowire active material, 20% ketjen black and 10% carboxy methyl cellulose (CMC aqueous solution). The mixed slurry was pasted on copper foil and dried in an oven at 70 °C for 12 h. Then, the metallic sodium foils were used as both the reference and counter electrodes. Whatman glass microfiber filter membrane as the separator, and the solution of 1 M trifluomethanesulfonate ($NaCF_3SO_3$) in diethyleneglycol dimethylether (DEGDME) as the electrolyte. Galvanostatic charge-discharge tests were performed at a potential range of 0.01–2 V vs. Na/Na^+ using a multichannel battery testing system (LAND CT2001A). Cyclic voltammetry (CV) was tested with an electrochemical workstation (Autolab PGSTAT).

3. Results and discussion

Crystal structure and morphology of as-prepared Sb_2Se_3 NWs are firstly checked carefully by TEM. Fig. 1a presents a low-magnification TEM image of Sb_2Se_3 NWs with diameters ranging from 20 to 80 nm. The one-dimensional Sb_2Se_3 NW with a smooth surface is identified to grow along the [001] direction as shown in Fig. 1b. Further high-resolution TEM (HRTEM) image in the inset in Fig. 1b shows ordered lattice fringes with spacing distances of 2.87 Å, corresponding to (221) and (-2-21) planes of orthorhombic Sb_2Se_3 (JCPDS: 15–0861, space group: *Pbnm*), respectively. The ED pattern in Fig. 1c can also be indexed as the orthorhombic Sb_2Se_3. All these reveal the single-crystalline feature of as-prepared Sb_2Se_3 NWs. Fig. 1d illustrates the atomic structure model of Sb_2Se_3. Each layer of orthorhombic Sb_2Se_3 has numerous packing structures, resulting in either trigonal prismatic or octahedral coordination of the Sb within the layered matrix of the Se [30–32]. The distance between chains is 3.29 Å [33,34], which is spacious enough to host most single-atom cations. Obviously, the 2D zigzag layered structure of Sb_2Se_3 allows Na ions (ionic radius: 1.02 Å [35]) to facilely diffuse. The energy dispersive X-ray spectroscopy (EDS) mapping in Fig. 1e not only demonstrates the uniform distribution of Sb and Se elements, but also indicates high purity of as-synthesized samples.

The nanosized SIBs that enable the real-time observation of the *in situ* electrochemical (de)sodiation process of individual Sb_2Se_3 NWs were constructed inside a TEM, as schematically shown in Fig. 2a. By applying a potential of −1.0 V to the NW with respect to the Na counter electrode, the sodiation of the NWs would be triggered from the point of contact with the Na resource. Fig. 2b−e show chronological TEM images of three

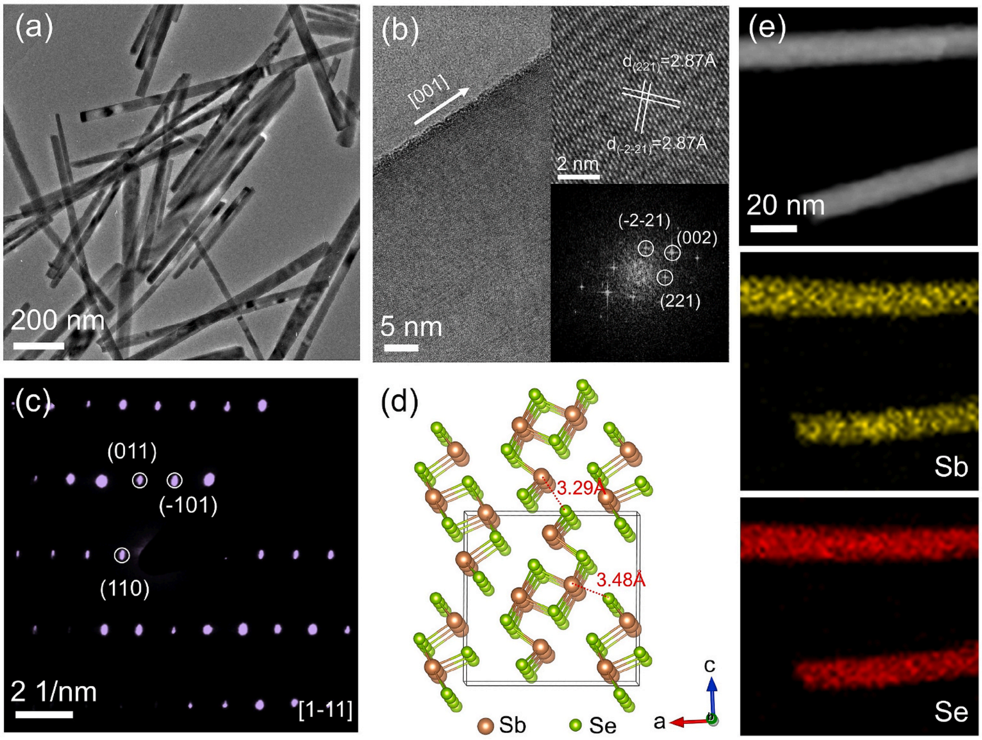

Fig. 1. (a) Low-magnification TEM image of as-synthesized Sb_2Se_3 NWs. (b) The magnified TEM images of the Sb_2Se_3 NW with an inset of the high-resolution TEM image and FFT. (c) ED pattern of a pristine Sb_2Se_3 NW, indicating good crystallinity and single crystal nature. (d) Crystal structure model of the orthorhombic Sb_2Se_3, showing that the minimum distance of two neighboring Sb_2Se_3 chains is 3.29 Å. (e) The HAADF image of pristine Sb_2Se_3 NWs and corresponding EDS element mappings.

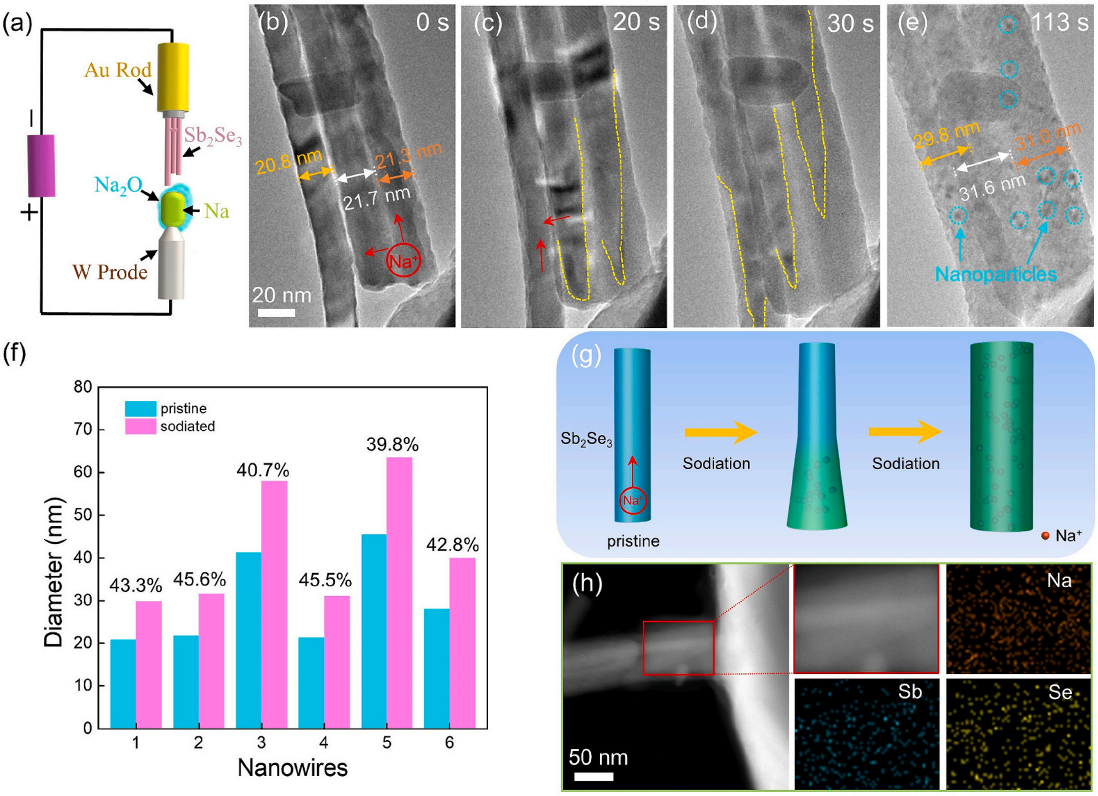

Fig. 2. (a) Schematic illustration of the experiment setup for *in situ* electrochemical sodiation and desodiation. (b–e) Chronological TEM images show morphological evolution of three Sb_2Se_3 NWs during the first sodiation process. Obvious volume expansion is visible. (f) Statistical results of radial expansion rate from six groups of *in situ* sodiation experiments. (g) Schematic illustration of morphological evolution during the first sodiation process of Sb_2Se_3 NW. (h) HAADF image of a sodiated Sb_2Se_3 NW and the corresponding EDS mappings of Na, Sb, and Se elements.

sodiating Sb_2Se_3 NWs (see also Movie S1 in Supporting Information), in which only the right and left NWs directly contacts the Na source. Upon sodiation, reaction fronts (RFs) marked with yellow dashed lines began to appear and gradually propagated along the NW axial direction in the form of V-shape, Fig. 2c. This indicates that Na ions diffused faster on the surface of the NWs. Note that although the middle NW did not directly contact Na source, it was also sodiated by the right and left NWs. Additional *in situ* experiments were carried out to further corroborate the unhindered lateral ionic transport pathway, as shown in Fig. S1 (see also Movie S2 in Supporting Information). The observed scenarios of facile, lateral transfer of Na ions between NWs in localized contact regions also indicated *a-b* plane diffusion within the NWs, as expected structurally. For the region of the NWs behind the RFs, distinct changes in the interior contrast were observed as well as substantial cross-sectional expansion, as shown in Fig. 2d.

Supplementary data related to this article can be found at https://doi.org/10.1016/j.nanoen.2020.105299.

After full sodiation at 113 s in Fig. 2e, numerous tiny nanoparticles appeared in NWs, characterized by a darker contrast. In particular, although the initial Na source was different, the resulting radial expansion rate (around 45%) of three NWs was essentially the same (from left to right: 20.8 nm → 29.8 nm, 21.7 nm → 31.6 nm, and 21.3 nm → 31 nm, respectively), indicating their similar degrees of sodiation. This value is convincing, as proved by the statistical results of another six groups of *in situ* experiments in Fig. 2f. Undoubtedly, such morphological changes resulted from electrochemical sodiation rather than beam-induced phase decomposition, as evidenced by repeated careful *in situ* experiments in Figs. S2 and S3 (see also Movie S3 and S4 in Supporting Information). Moreover, the elongation of a NW during sodiation can be estimated quantitatively from Fig. S1, in which one pristine NW was elongated from 627 nm to 714 nm within 38 s, corresponding to a ~13.8% elongation. Given that there is a Na-concentration gradient along the NW, the actual value may be higher than that. Schematic illustration in Fig. 2g vividly highlights aforementioned morphological evolutions during the whole sodiation process of a Sb_2Se_3 NW. Fig. 2h further shows the HAADF image of a NW after full sodiation and the corresponding EDS mappings, in which the evenly distributed Sb, Se, and Na elements were detected, implying that the entire NW underwent the same sodiation level.

Supplementary data related to this article can be found at https://doi.org/10.1016/j.nanoen.2020.105299.

To understand underlying sodiation mechanisms of Sb_2Se_3 NWs, we used the *in situ* HRTEM imaging to track localized phase structure in the vicinity of the RFs in real time. Fig. 3a–c show a moving sharp RF interface (marked with blue dashed lines) that divided the NW into two distinct regions along the axial direction. The region ahead of such an interface still remained clear lattice fringes, implying an intercalated region with $Na_xSb_2Se_3$ phase; while for the region behind the interface, the lattice fringes entirely disappeared, indicating a higher degree of sodiation far than the intercalation reaction. Fig. 3d, enlarged TEM image and corresponding FFT pattern further identified the formation of Na_2Se (JCPDS: 23–0527) crystals with clear (311) plane, indicating that conversion reaction had taken place in the highly sodiated region. A possible conversion reaction can be suggested as: $Na_xSb_2Se_3 + (6-x)$ $Na^+ + (6-x)\ e^{-1} \rightarrow 2Sb + 3Na_2Se$. As observed in another NW in Fig. 3e–i (see also Movie S5, Supporting Information), the newly formed Na_2Se phase is always found near the RF interface, irrespective of the RF shape. In addition, time-sequenced HRTEM images in Fig. 3e–i disclose that the formation of V-shaped RF should be attributed to faster conversion reaction along the radial (or [101]) direction of the NW than that along the axial direction.

Supplementary data related to this article can be found at https://doi.org/10.1016/j.nanoen.2020.105299.

Following the conversion reaction stage, the HRTEM was used to probe further sodiation reaction. As shown in Fig. 4, time-lapsed HRTEM images of localized regions and corresponding FFT patterns are arrayed in the ascending order of Na^+ content. After the conversion reaction, the intercalated Na ions displaced Sb in Sb_2Se_3, forming Na_2Se and Sb phases. Both HRTEM images and corresponding FFT patterns indicate the formation of Sb nanocrystals with the lattice fringe and diffraction spots that can be indexed to be (012) and (004) plane of Sb (JCPDS: 71–1173), Fig. 4c. With sodiation reaction going on, tiny NaSb (JCPDS: 74–0801) crystallites with (110) and (−102) planes were detected, Fig. 4d. Note that the NaSb phase existed only for a relatively short time and thus was missed easily. Obviously, the formation of NaSb phase indicates the alloying reaction between metal Sb and Na ions took place. Further alloying reaction produced the Na_3Sb phase (JCPDS: 74–1162) as the final sodiated product that could exist stably, Fig. 4e.

Consecutive *in situ* ED patterns that were not interrupted by HRTEM imaging were recorded as movie to better visualize the sequential structural evolutions during sodiation of the NW, as shown in Fig. 5a–e (see also Movie S6, Supporting Information). Upon initial sodiation (i.e., the intercalation stage) in Fig. 5b, the ED pattern shows noticeable changes with diffraction spots starting to become blurred, in contrast to

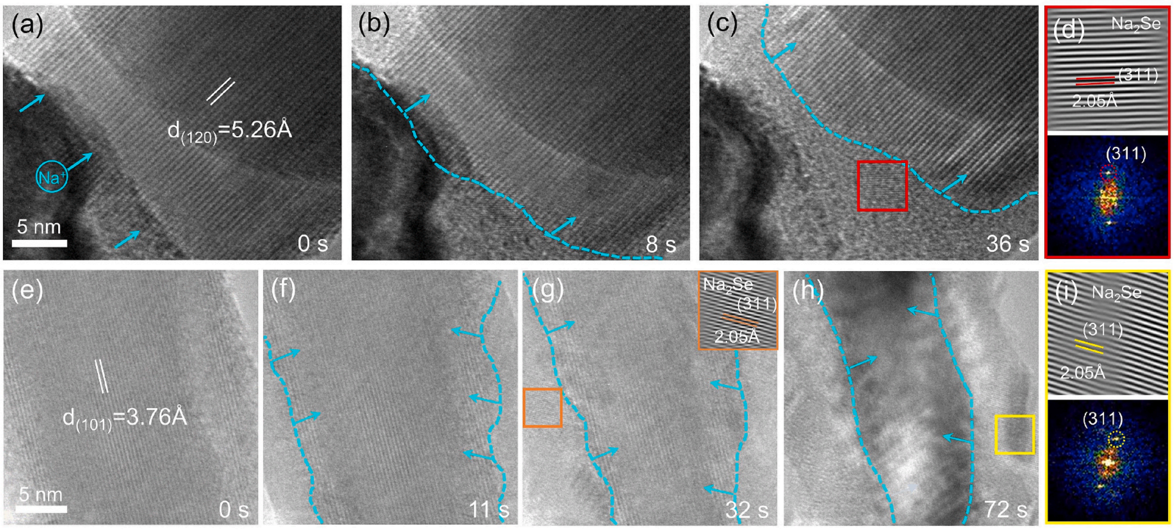

Fig. 3. (a–c) Snapshots of the Sb_2Se_3 NW during the sodiation process. (d) Filtered image and corresponding FFT patterns collected from the marked regions in (c). (e–h) Time-sequenced HRTEM images of the sodiation process of another Sb_2Se_3 NW. The inset filtered image in (g) is the enlargement of the region marked by orange box. (i) Filtered image and corresponding FFT patterns collected from the marked region in (h).

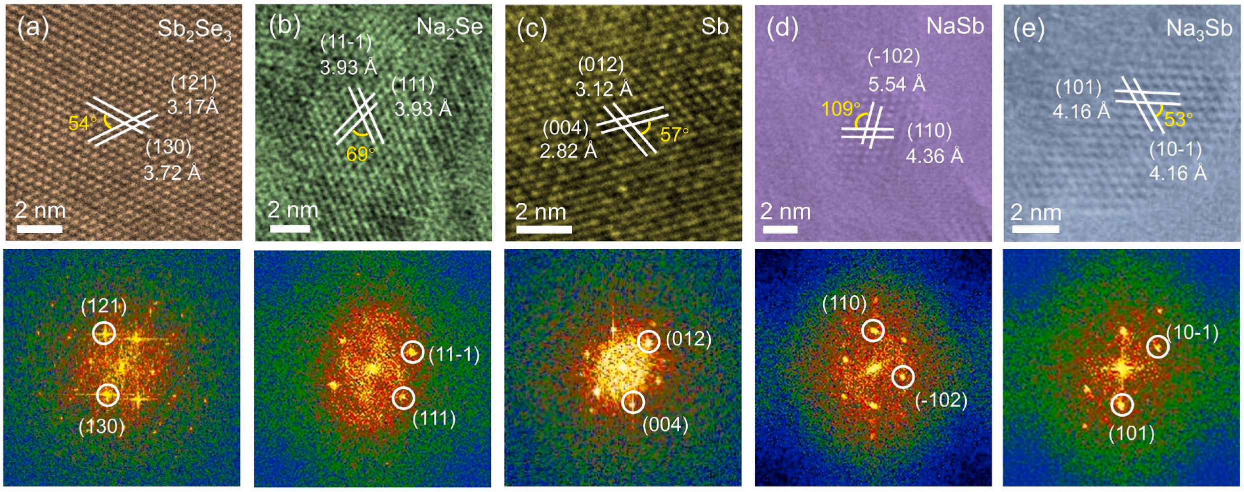

Fig. 4. HRTEM images and corresponding FFT patterns, demonstrating the sequential formation of Na_2Se, Sb, NaSb, and Na_3Sb phases during the whole sodiation process, respectively.

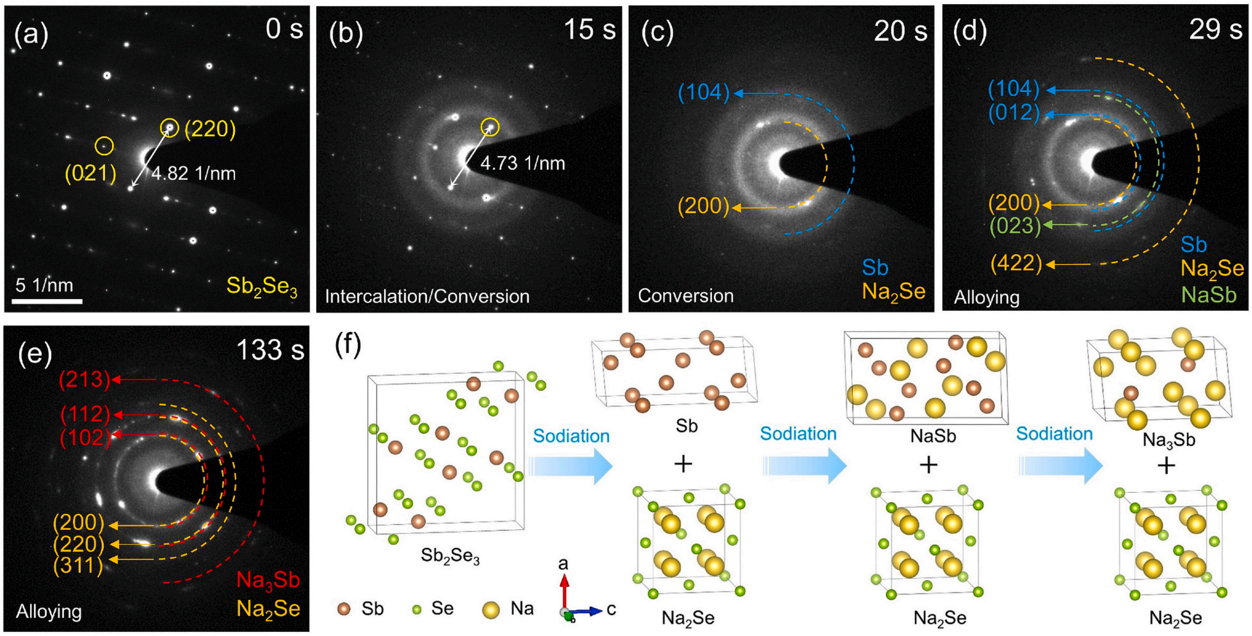

Fig. 5. (a–e) Consecutive ED patterns for identifying phase evolutions of Sb_2Se_3 NW during the whole sodiation process. (f) Atomic structure models of different sodiation stages corresponding to the phases formed during the first sodiation process.

bright and clear diffraction spots of pristine structure in Fig. 5a. The lattice spacing of (220) plane increased from 4.14 nm to 4.22 nm at 15 s, confirming the insertion of sodium ions. Meanwhile, some diffraction halos superimposed on diffraction spots developed, although they were quite diffuse, indicating the beginning of conversion reaction. These fine structural changes are difficult to be discerned by HRTEM imaging. Once the conversion reaction was completed, Fig. 5c, all the diffraction dots disappeared, and the diffraction halos, indexed as the (200) plane of Na_2Se and (104) plane of Sb, became brighter. As the sodiation stepped into the alloying reaction, the NaSb phase with the (023) plane appeared as well as more diffraction rings and spots indexed as Na_2Se and Sb (Fig. 5d), indicating the coexistence of three phases at this stage. As the as-formed Sb in the conversion reaction is completely alloyed with Na after 133 s (Fig. 5e), the ED patterns corresponding to Na_2Se and Na_3Sb phases never changed, indicating full sodiation of the NW. The final sodiated product is the mixture of Na_2Se and Na_3Sb phases, agreeing well with HRTEM observations.

Supplementary data related to this article can be found at https://doi.org/10.1016/j.nanoen.2020.105299.

Therefore, by combining *in situ* HRTEM imaging and consecutive ED patterns, the stepwise sodiation mechanism involving intercalation, conversion, and alloying reactions can be expressed by Equations (1)–(3). Atomic structure models for different phase evolution stages in the first sodiation process are also illustrated in Fig. 5f. It must be noted that the intermediate NaSb phase is indispensable in the alloying reaction, despite its transient presence.

$$\text{Intercalation reaction: } Sb_2Se_3 + xNa^+ + xe^{-1} \rightarrow Na_xSb_2Se_3 \tag{1}$$

$$\text{Conversion reaction: } Na_xSb_2Se_3 + (6-x)Na^+ + (6-x)\,e^{-1} \rightarrow 2Sb + 3Na_2Se \tag{2}$$

$$\text{Alloying reaction: } Sb + xNa^+ + xe^{-1} \rightarrow Na_xSb \ (x = 1-3) \tag{3}$$

After understanding fully multiple sodiation reaction pathways in Sb_2Se_3 NWs, it is urgently desired to reveal whether such NWs were none the less able to desodiate easily, and particularly, whether the desodiation could be transferred among the neighboring NWs, as the sodiation did. With these questions in mind, we intentionally designed a desodiation configuration, in which two presodiated NWs (NW1 and NW2) were laterally contacted, as shown in Fig. 6a. After a constant positive potential of 2.0 V was applied to initiate the desodiation, a distinct desodiation reaction front (DRF, marked by red arrows) immediately appeared, especially characterized by substantial cross-section contraction, and propagated longitudinally along NW1, Fig. 6b. After 28 s, the DRF from NW1 reached NW2 where a second desodiation pathway was bridged between them, Fig. 6c. Then, the DRF crossed the contact interface laterally, and continued to propagate longitudinally along NW2 until its terminal, Fig. 6d and e. The whole desodiation process was recorded in Movie S7, Supporting Information. By contrasting Fig. 6a and e, the extraction of Na ions directly led to obvious radial contraction of two NWs. However, their resulting contraction rates were relatively different (32% for NW2 from 53 nm to 36 nm and 18% for NW1 from 62 nm to 51 nm, respectively) and a lower desodiation degree was found for NW1.

Supplementary data related to this article can be found at https://doi.org/10.1016/j.nanoen.2020.105299.

Therefore, the ED was used to further distinguish phase evolutions of these two desodiating NWs. Upon desodiation, the ED patterns of NW2 attributed to Na_3Sb phase gradually disappeared and the Sb phase was detected again (Fig. 6g), implying that the dealloying reaction of Na_3Sb had begun. Such a Sb phase existed as tiny nanoparticles with clear lattice fringes, as observed by HRTEM in Fig. S4 (Supporting Information). As the desodiation progressed, the Na_3Sb alloy vanished thoroughly and was not detected by ED in the end, Fig. 6h, proving the full reversibility of dealloying reaction. For subsequent deconversion reaction, although the ED patterns and local HRTEM images identified the recovery of Sb_2Se_3 phase, the residual Na_2Se and Sb phases still existed in the finally desodiated product, implying an incomplete deconversion reaction, Fig. 6h and i.

Such a desodiation process can be exhibited vividly by schematic diagram in Fig. 6j. Ideally, the Sb metal and Na_2Se should be fully converted back to Sb_2Se_3 via the deconversion reaction. However, the dealloying of Na_3Sb took a long time and overlapped with the deconversion in the timescale during the entire desodiation process, which could result in residual Sb and isolated unusable “dead” Na owing to no sufficient time for subsequent desodiation [36]. Additionally, the driving force from the internal stress of recrystallization possibly caused the coarsening of Sb nanoparticles in the mixed Sb and Na_2Se phases, which further decreased the interface of deconversion reaction between these two phases and limited the Na diffusion, thus resulting in an incomplete conversion of Sb and Na_2Se to the original Sb_2Se_3 [37–42]. This point of view was also used to elucidate the example of SnS_2-based SIBs, in which only a part of Sn and Na_2S formed in the conversion reaction could be converted back to SnS_2 in the deconversion reaction [43]. Considering the deficiencies, previous reports have suggested that the operation of SIBs should be limited to only the intercalation and conversion reactions and avoid the alloying reaction at the expense of battery capacity [36].

By comparison, no Sb_2Se_3 phase was detected in ED patterns after

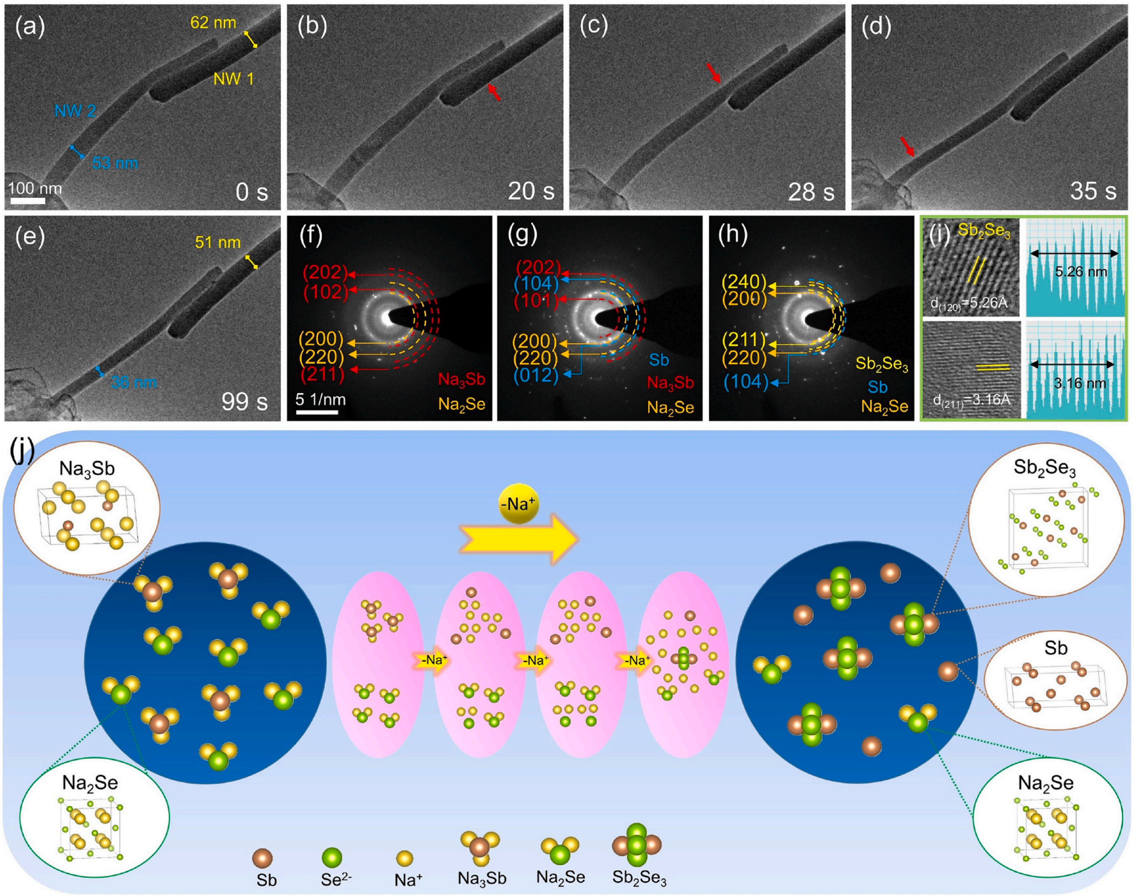

Fig. 6. (a−e) Microstructural evolutions of the Sb_2Se_3 NWs during the first desodiation process. (f−h) ED patterns used for identifying phase evolutions upon the first desodiation process of NW2. (i) HRTEM images of the fully desodiated NW2. (j) Schematic illustration of the desodiation stages corresponding to various phases upon an incomplete desodiation.

desodiation of NW1, Fig. S5 (Supporting Information), indicating that the deconversion of Na_2Se and Sb phases back to Sb_2Se_3 did not take place. This result agrees well with the preliminary judgment of the radial contraction rate observed in Fig. 6. In addition, during desodiation process of NW1, the phase transformation generated Sb and Se phases consistent with the previous report [44]. The indexed material phases are from the free Crystallography Open Database, and the detailed information about the crystal plane distances of each phase is clearly listed in Tables S1–6. The abnormal difference in desodiation degrees between these two lapped NWs enlightens us to think whether their contact interface played a role in the Na ions migration. Therefore, similar *in situ* experiments with laterally lapped NWs were repeated and further corroborated our conjecture, i.e., the existence of contact interface indeed hindered the deconversion reaction of the lapped NWs. This is because the NWs extracted and twisted all the time during desodiation, which inevitably resulted in unstable contact interface where electronic/ionic conductions were greatly impacted, resulting in sluggish electrode reaction kinetics. Contrast experiments only with a single NW undergoing desodiation were also conducted to verify the interface effect. Fig. 7a−k (see also Movie S8, Supporting Information) shows that even if a single NW was subjected to huge volume change and violent twisting upon multiple-cycle sodiation and desodiation processes, the partial deconversion reaction could still happen during desodiation, as judged by morphological observation and ED patterns (Fig. 7m–q). Fig. 7l further displays the specific expansion and contraction rates for each electrochemical sodiation-desodiation cycle. To the best of our knowledge, this is the first experimental visualization proof showing the effect of contact interface in nanostructured electrodes on phase transformations during desodiation. This new finding reminds us that special attention should be paid to interface engineering in a real battery, particularly with multistep reaction kinetics mechanisms, in which electronic/ionic conduction depends greatly on steady contact interfaces of electrode nanostructures.

Supplementary data related to this article can be found at https://doi.org/10.1016/j.nanoen.2020.105299.

To correlate the macroscopic electrochemical properties of Sb_2Se_3 NWs with the microcosmic *in situ* TEM observations, electrochemical testing was performed on Sb_2Se_3 NW-based coin-type half cells. In Fig. S6a (Supporting Information), the cyclic voltammograms (CV) profiles show that the pair of reduction/oxidation peaks at 1.05/1.51 V is related to the (de)conversion reaction of Sb_2Se_3, i.e., $Na_xSb_2Se_3 + (6-x)Na^+ + (6-x)e^{-1} \leftrightarrow 2Sb + 3Na_2Se$, while the pair of reduction/oxidation peaks at 0.45/0.71 V is ascribed to the (de)alloying reaction of Sb, i.e., $Sb + xNa^+ + xe^{-1} \leftrightarrow Na_xSb$ ($x = 1$–3). The alloying reaction of Sb to Na_3Sb results in two peaks: a dominant peak around ~0.45 V and a broad shoulder at ~0.68 V, suggesting a two-step alloying process from Sb to Na_3Sb: $Sb \rightarrow Na_xSb \rightarrow Na_3Sb$. These results are consistent with the *in situ* TEM observations, in which the conversion reaction is characterized by the appearance of Na_2Se and Sb phases and the alloying reaction of Sb and Na formed Na_3Sb phase via intermediate phases such as NaSb during sodiation process.

The charge-discharge voltage profiles of Sb_2Se_3 for the initial five cycles in a voltage window of 0.01–2.0 V (*vs.* Na/Na^+) at a current density of 100 mA g^{-1}, as shown in Fig. S6b. For the first discharge curve, a flat plateau at ~0.5 V and an inclined plateau at 0.5–1.0 V are visible. For the subsequent discharge processes, two plateaus at 0.5 and 1.1 V are observed, which is consistent with the CV results. While in the charge processes, a distinctive plateau at 0.6 V and a less obvious plateau at ~1.55 V can be observed. Further, Fig. S6b clearly shows the huge capacity loss during the first cycle and the gradual capacity decay during the subsequent cycles. This is also consistent with the *in situ* TEM observations for the first five sodiation/desodiation cycles, in which the

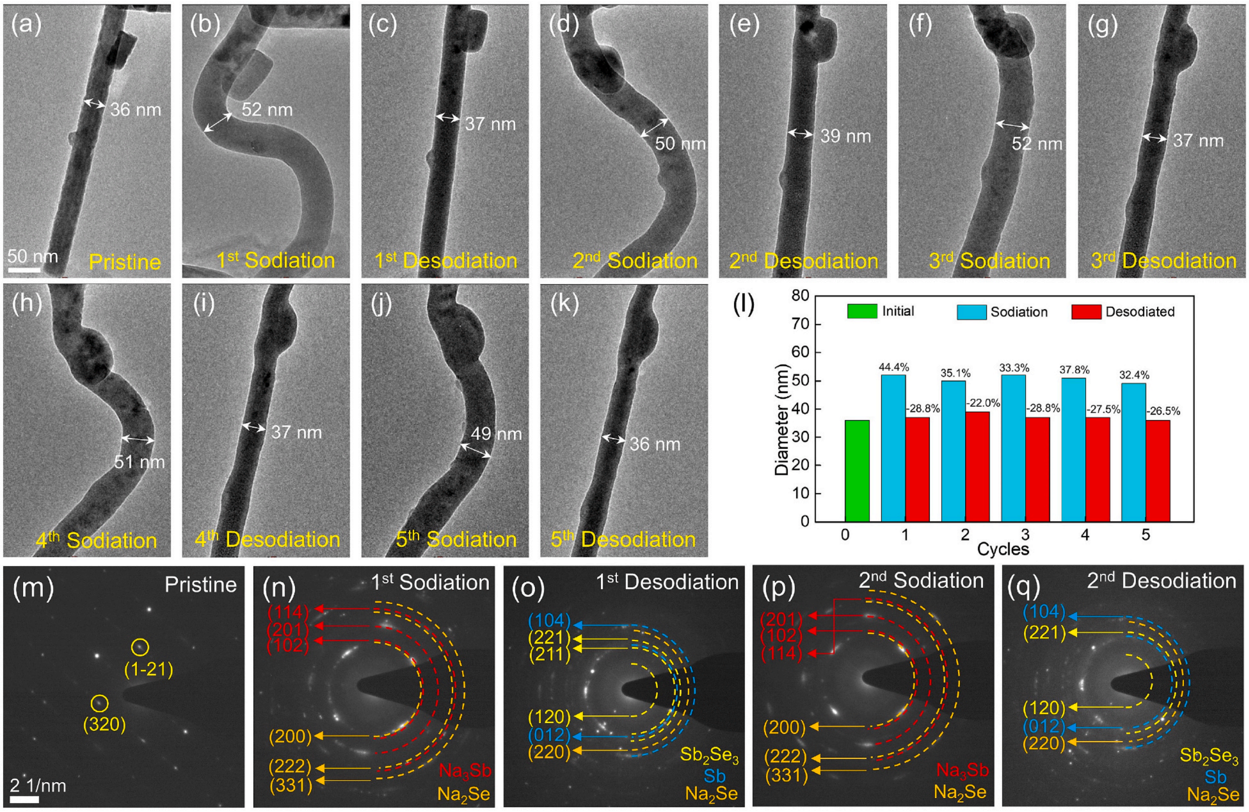

Fig. 7. (a−k) Microstructure evolutions of Sb_2Se_3 NW during the first five sodiation/desodiation processes. The NW exhibits multi-cycle reversible volume expansion and contraction with the insertion and extraction of sodium ions. (l) The measured diameters versus electrochemical cycling times of the Sb_2Se_3. The numeric percentages are for the diameter expansion/contraction during each event. (m−q) ED patterns show structural evolutions during the first two cycles of sodiation/desodiation processes of a Sb_2Se_3 NW.

largest volume change occurred in the first cycle. The cycling performance testing for 30 cycles at a current density of 100 mA g^{-1} is shown in Fig. S6c. The first discharge and charge capacities are 591 and 454 mA h g^{-1}, respectively, corresponding to a Coulombic efficiency of 76.8%. Capacity decay is observed in the cycling process and the discharge capacity fades to 312 mA h g^{-1} after 30 cycles. It should be noted, Sb_2Se_3 first accommodates the Na^+ intercalation, then undergoes a conversion reaction with Na, followed by an alloying process. Thus, one formula Sb_2Se_3 can accommodate 12 Na ions during the first discharge, delivering a high theoretical capacity of 670 mA h g^{-1}. While upon practical testing, the reaction (2) and (3) are assumed to be not totally reversible and hardly be distinguished. Therefore, the decreased specific capacity is a result of this two-step reaction coordination. Obviously, besides the possible formation of solid electrolyte interface (SEI) film [19,20], the partial irreversible phase transformation should be responsible for the irreversible capacity loss in the initial cycles, as proved by structural evolutions observed by the *in situ* TEM.

4. Conclusions

In conclusion, we have carefully investigated the whole (de)sodiation process of Sb_2Se_3 NW by combining *in situ* TEM imaging and consecutive ED sampling and proposed a new mechanism to delineate rapid capacity decay usually occurred in Sb_2Se_3 anodes. Consecutive ED patterns reveal that Sb_2Se_3 NWs underwent a three-step phase transformation during sodiation. Na ions were firstly intercalated into Sb_2Se_3 NWs, forming $Na_xSb_2Se_3$ phase; afterwards, continued Na intercalation initiated the conversion reaction, accompanied by the occurrence of Na_2Se and Sb phases; further, Sb could alloy with Na to form Na_3Sb phase via sequential intermediate Na_xSb phases. While during desodiation, in spite of reversible dealloying of Na_3Sb, the incomplete conversion of Na_2Se and Sb phases back to Sb_2Se_3 was considered to cause rapid capacity decay. The *in situ* experiment revealed that the unsteady contact interface of NWs greatly affects the degree of desodiaiton due to changed electrode reaction kinetics. This new finding reminds us that special attention should be paid to interface engineering in a real battery, particularly with multistep energy-storage mechanisms. More in-depth works regarding interface engineering, such as precise coating strategy during synthesis and preparation of electrode materials, will be essentially necessary. Our work not only reports the first experimental evidence of the effect of contact interfaces on phase evolutions of electrode materials, but also provides new insights into capacity decay mechanisms that will be beneficial for rational design of high-capacity SIBs with long cycling life.

Credit author statement

Y. Wu and F. Xu conducted all in situ experiments in Southeast University and prepared the manuscript. W. Luo and L.Q. Mai prepared the samples and performed the electrochemical measurements. Y. Wu, F. Xu, W. Luo, P. Gao, C.Y. Zhu, X.B. Hu, K. Qu, J. Chen and Y.Q. Wang carried out the data analysis. F. Xu and L.T. Sun directed this work. All authors contributed to writing and revision of the manuscript.

Declaration of competing interest

The authors declare that they have no known competing financial interests or personal relationships that could have appeared to influence the work reported in this paper.

Acknowledgements

This work was financially supported by the National Natural Science Foundation of China (Grant Nos. 51972058, 11774051, 61574034, 51372039, 61774033, and 61674029), the National Basic Research Program of China (973 Program, Grant No. 2015CB352106), the National Natural Science Foundation of Hubei Province (Grant No. 2019CFB195) and the Scientific Research Foundation of Graduate School of Southeast University (Grant No. YBPY2026). F. Xu thanks Shulin Chen from Peking University for his useful discussion.

Appendix A. Supplementary data

Supplementary data to this article can be found online at https://doi.org/10.1016/j.nanoen.2020.105299.

References

[1] M. Armand, J.M. Tarascon, Nature 451 (2008) 652–657.
[2] C.K. Chan, H. Peng, G. Liu, K. McIlwrath, X.F. Zhang, R.A. Huggins, Y. Cui, Nat. Nanotechnol. 3 (2008) 31–35.
[3] M.D. Slater, D. Kim, E. Lee, C.S. Johnson, Adv. Funct. Mater. 23 (2013) 947–958.
[4] H. Wang, S. Yuan, D. Ma, X. Zhang, J. Yan, Energy Environ. Sci. 8 (2015) 1660–1681.
[5] S. Yuan, Y.B. Liu, D. Xu, D.L. Ma, S. Wang, X.H. Yang, Z.Y. Cao, X.B. Zhang, Adv. Sci. 2 (2015), 1400018.
[6] T. Sun, Z. Li, H. Wang, D. Bao, F. Meng, X. Zhang, Angew. Chem. Int. Ed. 55 (2016) 10662–10666.
[7] J.B. Goodenough, J. Solid State Electrochem. 16 (2012) 2019–2029.
[8] J. Cabana, L. Monconduit, D. Larcher, M.R. Palacin, Adv. Mater. 22 (2010) E170–192.
[9] M.M. Rahman, Y. Xu, H. Cheng, Q. Shi, R. Kou, L. Mu, Q. Liu, S. Xia, X. Xiao, C. Sun, D. Sokaras, D. Nordlund, J. Zheng, Y. Liu, F. Lin, Energy Environ. Sci. 11 (2018) 2496–2508.
[10] C.Y. Zhu, F. Xu, H.H. Min, Y. Huang, W.W. Xia, Y.T. Wang, Q.Y. Xu, P. Gao, L. T. Sun, Adv. Funct. Mater. 27 (2017), 1606163.
[11] X. Xu, M. Yan, X. Tian, C. Yang, M. Shi, Q. Wei, L. Xu, L. Mai, Nano Lett. 15 (2015) 3879–3884.
[12] M. Gu, A. Kushima, Y. Shao, J.G. Zhang, J. Liu, N.D. Browning, J. Li, C. Wang, Nano Lett. 13 (2013) 5203–5211.
[13] X. Rui, H. Tan, Q. Yan, Nanoscale 6 (2014) 9889–9924.
[14] M.V. Reddy, G.V.S. Rao, B.V.R. Chowdari, Chem. Rev. 113 (2013) 5364–5457.
[15] S.H. Choi, Y.C. Kang, Nanoscale 8 (2016) 4209–4216.
[16] J. Zhang, Z. Zhang, Q. Li, Y. Qu, S. Jiang, J. Electrochem. Soc. 161 (2014) A2093–A2098.
[17] J. Duan, W. Zhang, C. Wu, Q.J. Fan, W.X. Zhang, X.L. Hu, Y.H. Huang, Nano Energy 16 (2015) 479–487.
[18] W. Li, M. Zhou, H.M. Li, K.L. Wang, S.J. Cheng, K. Jiang, Electrochem. Commun. 60 (2015) 74–77.
[19] W. Luo, A. Calas, C.J. Tang, F. Li, L. Zhou, L.Q. Mai, ACS Appl. Mater. Interfaces 8 (2016) 35219–35226.
[20] X. Ou, C.H. Yang, X.H. Xiong, F.H. Zheng, Q.C. Pan, C. Jin, M.L. Liu, K. Huang, Adv. Funct. Mater. 27 (2017), 1606242.
[21] J.Y. Huang, L. Zhong, C.M. Wang, J.P. Sullivan, W. Xu, L.Q. Zhang, S.X. Mao, N. S. Hudak, X.H. Liu, Science 330 (2010) 1515–1520.
[22] F. Xu, L.J. Wu, Q.P. Meng, M. Kaltak, J.P. Huang, J.L. Durham, M. Fernandez-Serra, L.T. Sun, A.C. Marschilok, E.S. Takeuchi, K.J. Takeuchi, M.S. Hybertsen, Y.M. Zhu, Nat. Commun. 8 (2017), 15400.
[23] M.T. McDowell, I. Ryu, S.W. Lee, C.M. Wang, W.D. Nix, Y. Cui, Adv. Mater. 24 (2012) 6034–6041.
[24] M. Gu, A. Kushima, Y.Y. Shao, J.G. Zhang, J. Liu, N.D. Browning, J. Li, C.M. Wang, Nano Lett. 13 (2013) 5203–5211.
[25] E.R. Adkins, T.Z. Jiang, L.L. Luo, C.M. Wang, B.A. Korgel, ACS Energy Lett 3 (2018) 2829–2834.
[26] F. Xu, Z.R. Li, L.J. Wu, Q.P. Meng, H.L.L. Xin, J. Sun, B.H. Ge, L.T. Sun, Y.M. Zhu, Nano Energy 30 (2016) 771–779.
[27] Y. Wu, X.M. Xu, C.Y. Zhu, P.C. Liu, S.Z. Yang, H.L.L. Xin, R. Cai, L.B. Yao, M. Nie, S. Y. Lei, P. Gao, L.T. Sun, L.Q. Mai, F. Xu, ACS Energy Lett 4 (2019) 2081–2090.
[28] J. Ma, Y. Wang, Y. Wang, Q. Chen, J. Lian, W. Zheng, J. Phys. Chem. C 113 (2009) 13588–13592.
[29] W. Luo, A. Calas, C.J. Tang, F. Li, L. Zhou, L.Q. Mai, ACS Appl. Mater. Interfaces 8 (2016) 35219–35226.
[30] N.W. Tideswell, F.H. Kruse, J.D. Mccullough, Acta Crystallogr. 10 (1957) 99–102.
[31] R. Vadapoo, S. Krishnan, H. Yilmaz, C. Marin, Phys. Status Solidi B 248 (2010) 700–705.
[32] X. Ma, Z. Zhang, X. Wang, S. Wang, F. Xu, Y. Qian, J. Cryst. Growth 263 (2004) 491–497.
[33] H.B. Song, T.Y. Li, J. Zhang, Y. Zhou, J.J. Luo, C. Chen, B. Yang, C. Ge, Y.Q. Wu, J. Tang, Adv. Mater. 29 (2017), 1700441.
[34] C. Chen, K.H. Li, S.Y. Chen, L. Wang, S.C. Lu, Y.H. Liu, D.B. Li, H.S. Song, J. Tang, ACS Energy Lett 3 (2018) 2335–2341.
[35] J.Y. Hwang, S.T. Myung, Y.K. Sun, Chem. Soc. Rev. 46 (2017) 3529–3614.
[36] S.K. Kim, Z.P. Yao, J.M. Lim, M.C. Hersam, C. Wolverton, V.P. Dravid, K. He, Adv. Mater. 30 (2018), 1804925.
[37] X. Ou, L. Cao, X.H. Liang, F.H. Zheng, H.S. Zheng, X.F. Yang, J.H. Wang, C.H. Yang, M.L. Liu, ACS Nano 13 (2019) 3666–3676.
[38] R. Hu, H. Zhang, Z. Lu, J. Liu, M. Zeng, L. Yang, B. Yuan, M. Zhu, Nano Energy 45 (2018) 255–265.

[39] R. Hu, D. Chen, G. Waller, Y. Ouyang, Y. Chen, B. Zhao, B. Rainwater, C. Yang, M. Zhu, M. Liu, Energy Environ. Sci. 9 (2016) 595–603.
[40] W. Kang, Y. Wang, J. Xu, J. Mater. Chem. A 5 (2017) 7667–7690.
[41] J. Wang, L. Wang, C. Eng, J. Wang, Adv. Energy Mater. 7 (2017), 1602706.
[42] R. Hu, Y. Ouyang, T. Liang, X. Tang, B. Yuan, J. Liu, L. Zhang, L. Yang, M. Zhu, Energy Environ. Sci. 10 (2017) 2017–2029.
[43] X. Ou, L. Cao, X.H. Liang, F.H. Zheng, H.S. Zheng, X.F. Yang, J.H. Wang, C.H. Yang, M.L. Liu, ACS Nano 13 (2019) 3666–3676.
[44] Q.Q. Li, P.S. Du, Y.F. Yuan, W.T. Yao, Z.T. Ma, B.K. Guo, Y.C. Lyu, P. Wang, H. T. Wang, A. Nie, R. Shahbazian-Yassar, J. Lu, Nano Lett. 19 (2019) 3074–3082.

Yi Wu is currently pursuing her Ph.D. degree at Key Laboratory of MEMS of Education, Southeast University, Nanjing. She received her Bachelor's degree in Physics and Materials Science from Anhui University in 2016. Her research interests involve the design and synthesis of functional materials for energy storage and *in situ* study of lithium/sodium-ion batteries.

Dr. Wen Luo received her Ph.D. degree in 2018 from School of Materials Science and Engineering at Wuhan University of Technology under the supervision of Prof. Liqiang Mai. She was a visiting graduate student (2016–2017) in Prof. Jean-Jacques Gaumet Research Group at Université de Lorraine, France. She is currently an assistant professor at the Department of Physics, School of Science, Wuhan University of Technology. Her research focuses on nanomaterials and devices for energy storage and conversion.

Dr. Peng Gao is currently a Professor in School of Physics, Peking University, Beijing, China. He received his Ph.D. degree in 2010 from the Institute of Physics, Chinese Academy of Sciences. He was a post-doctoral fellow in University of Michigan (2010–2013), a research associate in Brookhaven National Laboratory (2013–2014), and a research fellow in University of Tokyo (2014–2015). He was selected in Project of Thousand Youth Talents and then joined in Peking University in 2015. His research interests include electron microscopy, ferroelectrics, solid-state ionics, and structure and properties of crystal defects and interfaces.

Dr. Chongyang Zhu received his BS from Nanjing University of Posts and Telecommunications in 2013 and PhD in 2019 at Key laboratory of MEMS of Ministry of Education, Southeast University. Now, he works as a postdoctoral fellow in Nano-Pico Center of Southeast University with research interests in the synthesis and applications of 2D materials for energy storage and conversion systems, as well as *in situ* TEM study of lithium/sodium-ion batteries.

Dr. Xiaobing Hu is currently an Assistant Professor in the School of Materials Science and Engineering, Northwestern University (NU), Evanston, USA. He obtained his Ph.D. in 2015 from Institute of Metal Research, Chinese Academy of Sciences. He was a Research Associate at Brookhaven National Laboratory from 2016 to 2018. His current research interests focus on advanced applications of TEM on materials science including engineering alloys, structural ceramics and energy storage materials.

Dr. Ke Qu received her Ph.D. degree in Condensed Matter Physics from Lanzhou University in 2018. Now, she has joined Shenzhen Institutes of Advanced Technology, Chinese Academy of Sciences, as a postdoctoral. Her research focuses on the atomic resolution structure and electronic structure evolution of transition metal oxides in-situ Cs-corrected transmission electron microscopy.

Dr. Jing Chen is an Associate Professor in the School of Electronic Science and Engineering, Southeast University (SEU), Nanjing, China. She obtained his Ph.D. in 2011 from Southeast University. In 2015, she was promoted to Associate Professor. Currently, her research interests focus on synthesis of domain quantum dot materials and quantum dot optoelectronic devices.

Dr. Yuqiao Wang is a Professor in the School of Chemistry and Chemical Engineering, Southeast University (SEU), Nanjing, China. He obtained his BS and Ph.D. from Anhui University and Southeast University, respectively. His current research interests include nanostructured photoelectric functional material and device integration, design and assembly of new energy materials, electron transport mechanism of interface and surface during photoelectric conversion and storage.

Dr. Litao Sun is currently a Distinguished Professor at Southeast University, Nanjing, China. He received his Ph.D. from the Shanghai Institute of Applied Physics, Chinese Academy of Sciences, followed by postdoctoral research at University of Mainz, Germany and a visiting professorship at the University of Strasbourg, France. His current research interests include *in situ* experimentation inside the electron microscope, graphene and related 2D materials, new phenomena from sub-10 nm nanoparticles, and applications of nanomaterials in environment, energy, and nanoelectromechanical systems.

Dr. Liqiang Mai is Chair Professor of Materials Science and Engineering at Wuhan University of Technology (WUT). He is Changjiang Scholar Professor, Distinguished Young Scholar of the National Science Fund of China. He received his Ph.D. from WUT in 2004 and carried out his postdoctoral research in the laboratory of Prof. Zhonglin Wang at Georgia Institute of Technology in 2006–2007. He worked as advanced research scholar in the laboratory of Prof. Charles M. Lieber at Harvard University in 2008–2011. His current research interests focus on nanomaterials and devices for energy storage.

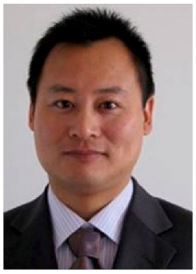

Dr. Feng Xu is a Professor in the Key Laboratory of MEMS of the Ministry of Education, Southeast University (SEU), Nanjing, China. He obtained his Ph.D. in 2009 from Nanjing Tech University. In 2012 and 2017, he was promoted to Associate Professor and Professor, respectively. He was a Visiting Scholar at Brookhaven National Laboratory from 2014 to 2015. Currently, he concentrates on study of structure-property relationship of nanomaterials, including but not limited to energy conversion and storage materials, by using *in situ* transmission electron microscopy.